

# The Underwater Backscatter Channel: Theory, Link Budget, and Experimental Validation

Waleed Akbar\*

wakbar@mit.edu

Massachusetts Institute of Technology  
Cambridge, Massachusetts, USA

Ahmed Allam\*

allam@mit.edu

Massachusetts Institute of Technology  
Cambridge, Massachusetts, USA

Fadel Adib

fadel@mit.edu

Massachusetts Institute of Technology  
Cambridge, Massachusetts, USA

## ABSTRACT

Underwater backscatter is a recent networking technology that enables net-zero-power communication and sensing in underwater environments. Existing research on underwater backscatter has focused on designing and demonstrating early systems with impressive capabilities; however, what remains critically missing is an end-to-end analysis of the underwater backscatter communication channel, which is necessary to understand the potential of this technology to scale to real-world applications and practical deployments.

This paper presents the first comprehensive theoretical and empirical analysis of the underwater backscatter channel, including the downlink and uplink of end-to-end backscatter. We introduce a closed-form analytical model that encompasses the physical properties of piezoelectric materials, electromechanical coupling, electrical impedance, and the underwater acoustic channel. We verify the correctness of this theoretical analysis through both finite-element-model physical simulations and real-world experimental validation in a river, demonstrating that the analytical model matches our real-world experiments with a median deviation of only 0.76 dB. Using this model, we then simulate the theoretical limits of underwater backscatter as a function of different design parameters and identify pathways for pushing underwater backscatter toward its theoretical limits.

## CCS CONCEPTS

- Networks → Physical links; Mobile networks;
- Applied computing → Earth and atmospheric sciences;

## KEYWORDS

Subsea IoT, Link Budget, Underwater Networks, Backscatter

\*Both authors contributed equally to this research.

Permission to make digital or hard copies of part or all of this work for personal or classroom use is granted without fee provided that copies are not made or distributed for profit or commercial advantage and that copies bear this notice and the full citation on the first page. Copyrights for third-party components of this work must be honored. For all other uses, contact the owner/author(s).

ACM MobiCom '23, October 2–6, 2023, Madrid, Spain

© 2023 Copyright held by the owner/author(s).

ACM ISBN 978-1-4503-9990-6/23/10.

<https://doi.org/10.1145/3570361.3613265>

## ACM Reference Format:

Waleed Akbar, Ahmed Allam, and Fadel Adib. 2023. The Underwater Backscatter Channel: Theory, Link Budget, and Experimental Validation. In *The 29th Annual International Conference on Mobile Computing and Networking (ACM MobiCom '23), October 2–6, 2023, Madrid, Spain*. ACM, New York, NY, USA, 15 pages. <https://doi.org/10.1145/3570361.3613265>

## 1 INTRODUCTION

Recent years have seen mounting interest in low-power, distributed subsea internet-of-things (IoT) networks because of their potential in environmental, industrial, and defense applications [1–6]. Energy-efficient ocean IoT networks can enable long-term sensing of ocean variables (temperature, pH, pressure, salinity, etc.) to create more accurate climate and weather prediction models and monitor the impact of climate change on the ocean [7, 8]. Similarly, low-cost and efficient ocean IoT networks can help boost the growth of the world’s blue economy by enabling active monitoring of marine infrastructures ranging from oil/gas pipelines to underwater tunnels [9]. Real-time distributed underwater sensor networks can help boost aquaculture (seafood farm) production by monitoring the farm vitals (water temperature, dissolved nutrients, pH, etc.) and detecting environmental hazards (such as harmful algae blooms) early [10]. Major industrial players, including Google, Microsoft, and Honeywell, have also become interested in deploying such networks to monitor underwater infrastructures (ranging from submerged data centers to gas and oil pipelines) and to develop sophisticated fish farming technologies [5, 11].

One recent technology that promises to deliver on the vision of low-cost, low-power subsea IoT networks is underwater piezo-acoustic backscatter [12–15]. Unlike traditional underwater acoustic communication, piezo-acoustic backscatter communicates information via reflection of external acoustic signals (instead of generating its own carrier),<sup>1</sup> which enables backscatter sensor nodes to sense and communicate at five to six orders of magnitude lower power than state-of-the-art underwater modems, even at similar data rates [12]. While the initial demonstrations of backscatter communication are encouraging, the theoretical and practical limits of underwater backscatter are largely unknown. Specifically, recent work on backscatter has shown that it is

<sup>1</sup>This also eliminates the need for a power-amplifier at the sensor.

possible to achieve a few to tens of meters of operation range but it remains unclear how the achievable range is related to the system's parameters - such as input power, operating frequency, electrical matching, transducer design, etc. - and whether the range of operation can indeed be extended to deploy this technology at scale in practical environments, such as coastal, offshore, and/or deep-sea environments.

In this paper, we present the first end-to-end link-budget analytical model to characterize the theoretical limits of underwater backscatter. The model captures the impact of system parameters on the operation range - downlink power-up range and uplink communication range - and accurately predicts the theoretical achievable limits of piezo-acoustic backscatter under practical constraints. The analytical model presents a generalizable framework - independent of geometrical and operational assumptions - for the design and characterization of underwater backscatter.

Before introducing our link-budget analytical model, it is important to understand why the existing link-budget models for RF-backscatter and point-to-point underwater acoustic communication cannot be used to study underwater backscatter. RF backscatter link-budget analysis is well-established and has been extensively used to characterize and study RF backscatter networks, such as RFIDs [16, 17]. This analysis, however, cannot be easily extended to underwater backscatter systems because of the electromechanical properties of underwater backscatter nodes. Specifically, unlike in-air RF systems, underwater systems typically rely on acoustic waves to communicate. Thus, underwater backscatter leverages piezo-electric transducers to transmit and receive acoustic signals, and these transducers convert *mechanical* acoustic waves to *electrical* signals and vice versa [12]. This electro-mechanical coupling is unique to underwater backscatter, and it enables backscatter communication by translating the electrical switching signal to different pressure levels of the traveling acoustic wave. RF-backscatter, on the other hand, relies on antennas to communicate, and these antennas translate electrical signals to different levels of the traveling electromagnetic wave. As a result, past work on link budget analysis of RF backscatter cannot capture the electro-acoustic transduction of underwater backscatter. Similarly, traditional point-to-point acoustic underwater communication analytical models [18, 19] are also insufficient for characterizing underwater backscatter communication as these models do not rely on *reflection* for communication. Therefore, these models cannot explain the relationship between the electrical impedance switching of a backscatter node and the signal-to-noise ratio (SNR) of the received backscattered signal.

To overcome the shortcomings of existing link budget models and capture the phenomenon of electro-acoustic transduction, we develop an analytical model that unpacks

the entire path of signal propagation in underwater backscatter communications. Our derivation of the model starts from the input electrical power at the projector (transmitter) and concludes with the SNR of the backscattered signal at the hydrophone (receiver). We use the first principles of underwater acoustics and circuit theory to derive a relationship for downlink harvested power as a function of input electrical power, transducers' parameters (electromechanical efficiency and directivity), path loss due to the underwater channel, and electrical impedance mismatch at the backscatter node. To capture the effect of switching on the uplink communication, we derive a relationship for *differential scattering cross-section* - analogous to differential radar cross-section in RF-backscatter [20] - of the backscatter node that relates the change in electrical impedances (i.e., switching between ON-OFF) to two distinct pressure levels of the reflected acoustic waves. These different pressure levels are then translated to SNR at the hydrophone.

Since the goal of the analytical modeling is to enable the characterization and understanding of underwater backscatter, we take our analytical model one step further and reduce the theoretical terms to experimentally measurable quantities. For instance, we reduce the reflection coefficient (defined in terms of electro-acoustic impedances) to the backscatter node's efficiency and electrical mismatch loss. This reduction is important because it allows us to develop a plug-and-play model that accurately predicts the achievable operation ranges for given experimental conditions.

We verified our analytical framework for the underwater backscatter model through both numerical simulation and experimental validations. We developed an end-to-end backscatter high-fidelity numerical model in COMSOL Multiphysics [21] for both spherical and cylindrical underwater transducers. We also fabricated an in-house backscatter node and a projector, using cylindrical piezoelectric transducers. We performed experiments for both downlink energy harvesting and end-to-end backscatter in a river. Our results demonstrate the following:

- The end-to-end underwater backscatter operation can be represented in a closed-form analytical model that accounts for the various electrical, mechanical, and acoustic system parameters. This model is verified through physics-based numerical simulations, with a median error less than 0.4 dB across the simulated frequencies.
- The numerical simulations demonstrate that our model is generalizable and it accurately tracks the backscatter performance regardless of the transducer's shape and size. Additionally, our empirical evaluation in the river demonstrates that our experimental results from real-world testing match the analytical model, with a median error of less than 0.76 dB across frequencies, further validating the model empirically.

- We use our model to show that underwater backscatter technology, in principle, is scalable to kilometer-long distances under certain design parameters, and therefore, it offers a viable pathway to deliver on the vision of Ocean IoT in a number of key applications.

**Contributions.** This paper presents the first end-to-end theoretical and practical analysis of underwater backscatter. It contributes a closed-form analytical solution of the underwater backscatter channel that accounts for the various electrical, mechanical, and acoustic properties of such systems. It also contributes a numerical validation of this analytical model through finite-element-model physics simulations and an empirical validation through implementing and evaluating a backscatter system in real underwater environments. Finally, the paper outlines how this model can be used to design systems that extend underwater backscatter to its theoretical limits.

By introducing the first end-to-end analytical model of underwater backscatter, this paper takes an important step in filling a gap in the existing literature on underwater backscatter with a validated theoretical framework. We hope that this will open the door for researchers and practitioners to propel the field forward, similar to how RF backscatter / RFID systems have advanced over the past two decades through the combination of system building and theoretical advances.

## 2 LINK-BUDGET THEORY

The overall architecture of a canonical underwater backscatter system is shown in Fig. 1. The system encompasses a transmitter (Tx) that sends a signal on the downlink to the backscatter node. The backscatter node communicates data by modulating the reflections of this downlink signal. A hydrophone receiver (Rx) senses the modulated reflections and uses them to decode the data transmitted by the backscatter node. The backscatter node can also harvest energy from the downlink signal to power up. Throughout our derivation, we assume that the distance between Tx and the backscatter node is large enough to adopt far-field approximations (which is typical for underwater operation). For simplicity, we focus on a single backscatter node, but the same analysis generalizes to any number of nodes in the environment.

The goal of our theoretical modeling is to derive a closed-form analytical expression of the backscatter channel starting from the input electrical power to Tx ( $P_{elec}$ ) to the signal-to-noise ratio (SNR) of the backscatter signal at the hydrophone (Rx). We do this in three key steps:

- First (in §2.1.1), we define a general expression for modeling the acoustic transducer (used as Tx, Rx, and backscatter node) that captures its electromechanical coupling.
- Second (in §2.2), we derive the downlink model starting from the input electrical power at the Tx to the energy harvested by the backscatter node ( $P_{harv}$ ).

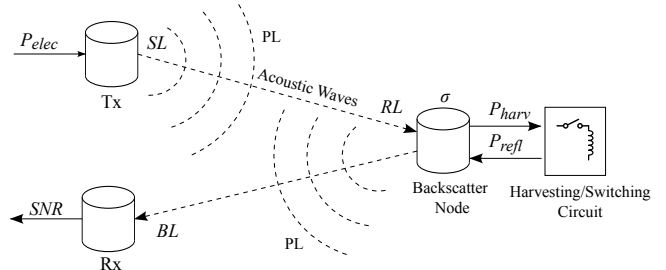


Figure 1: Canonical Underwater Backscatter Architecture.

- Finally (in §2.3), we derive the uplink model for the backscatter SNR as a function of different system parameters including  $P_{elec}$  and Tx, Rx, and backscatter transducer characteristics. To complete the uplink model, we derive expressions for the scattering cross-section ( $\sigma$ ) of the node and the backscattered pressure level ( $BL$ ).

In the subsequent sections, we validate these models through numerical simulations and experimental evaluation.

### 2.1 Modeling the piezoelectric transducer

We describe two models of piezoelectric transducers for our analytical formulation and numerical validation.

**2.1.1 Classical Equivalent Circuit Model.** A piezoelectric transducer is commonly approximated with its equivalent circuit parameters [22] as shown in Fig. 2a. The lumped elements represent the electrical properties (static capacitance  $C_o$ ), mechanical properties (equivalent mass  $M_m$  and equivalent stiffness  $C_m$ ), piezoelectric properties (transformer ratio  $\phi$ ), and acoustic properties (radiation impedance  $Z_r = R_r + jX_r$ ). The representation also accounts for the transducers' dielectric loss ( $G_o$ ) and mechanical loss ( $R_m$ ). The values of the equivalent parameters can be derived from the transducer's geometry and material properties for a small set of idealized transducers (e.g. a spherical transducer), but most commonly, they are evaluated from numerical simulations [23]. The mechanical force acting on the transducer's surface due to the incident acoustic pressure is commonly referred to as the blocked force ( $F_b$ ). Generally, the  $F_b$  is not uniform across the surface, and its value is calculated by integrating the total acoustic pressure field over the transducer's surface. Assuming a uniform incident pressure field (plane wave) with a root-mean-square (rms) pressure of  $\bar{p}_i(\Omega)$ , the total rms force acting on the transducer is given by [22]:

$$F_b(\Omega) = D_a(\Omega) A \bar{p}_i(\Omega) \quad (1)$$

where  $A$  is the active surface area of the transducer,  $D_a(\Omega)$  is its diffraction constant, and  $\Omega$  is the solid angle between incident pressure wave and the transducer's main axis. The diffraction constant is a measure of the pressure field disturbance caused by the transducer and is given by [22]:

$$D_a(\Omega)^2 = \frac{4\pi c R_f D_f(\Omega)}{\rho w^2 A^2} \quad (2)$$

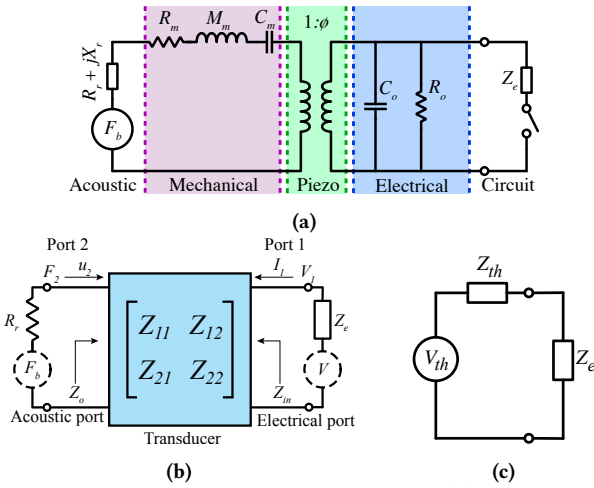


**Figure 2: Transducer Circuit Representations.** (a) shows a lumped circuit model using circuit elements to represent electro-acoustic properties. (b) shows the equivalent 2-port network Z-parameters representation of the same circuit. (c) shows the Thevenin equivalent model at Port 1.

where  $c$  and  $\rho$  are the speed of sound and mass density of water<sup>2</sup>.  $D_f(\Omega)$  is the directivity factor of the transducer.  $D_f$  and  $R_r$  can be expressed analytically for transducers with simple geometries (e.g. spherical transducer, baffled piston transducer), but they are commonly calculated numerically.

**2.1.2 Simplified General Model.** The equivalent circuit model described above is useful for designing transducers that operate around their fundamental resonance, however, it is not suitable for transducers operating beyond their resonance. To derive a closed-form expression of backscatter, we define a more general equivalent circuit model (and recast this model in §3 in terms of the classical model described above for completeness).

For a general circuit model of a transducer, we represent it as a 2-port element with acoustical and electrical ports. Fig. 2b shows the two-port representation of the transducer with port-1 connected to an electrical load  $Z_e$  and port-2 connected to the acoustic radiation load  $R_r$ . If there is incident acoustic pressure on the node, it is represented by  $F_b$ , and similarly, an electrical voltage  $V$  can be applied on the electrical port of the transducer (e.g. when used as Tx). The transducer equivalent impedance looking from the electrical and acoustic sides are  $Z_{in}$  and  $Z_o$ , respectively. We represent this 2-port element with an impedance matrix<sup>3</sup>, defined as:

$$\begin{bmatrix} V_1 \\ F_2 \end{bmatrix} = \begin{bmatrix} Z_{11} & Z_{12} \\ Z_{21} & Z_{22} \end{bmatrix} \begin{bmatrix} I_1 \\ u_2 \end{bmatrix} \quad (3)$$

<sup>2</sup>Note that  $c$  and  $\rho$  vary with temperature, salinity, and pressure in the vicinity of the transducer. However, these small variations (typically less than 5% of the nominal values  $c = 1480m/s$  and  $\rho = 1000kg/m^{-3}$ ) have a limited effect on the transducer dynamics.

<sup>3</sup>Note that this impedance matrix is a linear transformation from the more common ABCD matrix representation of underwater transducers [22].

where  $V_1$  and  $I_1$  are the voltage and current at the transducer's electrical terminal and  $F_2$  and  $u_2$  are the force and the velocity at the external surface of the transducer. In this representation, the impedance matrix accounts for all the transducer's parameters (including the acoustic radiation reactance,  $X_r$ ). It is also noted that all the physical variables are represented in rms unless otherwise stated.

## 2.2 Downlink Channel

To model the downlink channel, we analyze the signal path from the electrical source at Tx to the harvesting component in the backscatter node. We first calculate the conversion of electrical power to acoustic power in Tx, then model the propagation of acoustic waves in the water channel, derive the received acoustic level at the backscatter node  $RL$ , and finally calculate the harvested power by the backscatter node.

**2.2.1 Electrical to acoustic power.** The electromechanical efficiency ( $\eta_{Tx}$ ) of a transducer captures its ability to convert electrical energy to acoustic energy:

$$\eta_{Tx} = \frac{P_{ac}}{P_{elec}}, \quad (4)$$

where  $P_{ac}$  is the output acoustic power from the transducer, and  $P_{elec}$  is the input electrical power. Using the 2-port network of Fig. 2b,  $P_{elec}$  is given by:

$$P_{elec} = \frac{|V_1|^2 R_{in}}{|Z_{in}|^2} \quad (5)$$

where  $Z_{in} = R_{in} + jX_{in}$  is the input electrical impedance of the transducer and is a function of Z-parameters [24]:

$$Z_{in} = Z_{11} - \frac{Z_{12}Z_{21}}{Z_{22} + R_r} \quad (6)$$

Similarly, we can also express  $P_{ac}$  using the 2-port Z-network:

$$P_{ac} = \frac{|F_2|^2}{R_r} \quad (7)$$

By using Eq. 3, we can express output force  $F_2$  as:

$$F_2 = Z_{21}I_1 + Z_{22}u_2 \quad (8)$$

where  $I_1 = V_1/Z_{in}$  and  $u_2 = -F_2/R_r$ . Substituting Eqs. 5,6,7, and 8 in Eq. 4 yields:

$$\eta_{Tx} = |Z_{21}|^2 \frac{R_r}{R_{in}} \left| \frac{1}{R_r + Z_{22}} \right|^2 \quad (9)$$

The above equation shows that  $\eta_{Tx}$  can be represented as a function  $R_r$ ,  $R_{in}$ , and Z-parameters, and this representation of efficiency will help us simplify our link-budget analysis as we show in the following sections.

**2.2.2 From acoustic power to source level.** In underwater acoustics, the far-field pressure level generated by a transducer is defined as the source level ( $SL$ ).  $SL$  is a function of input electrical power ( $P_{elec}$ ) in Watts, electromechanical efficiency of the transducer ( $\eta_{Tx}$ ), and the transducer's directivity index ( $DI$ ) measured in dB.  $SL$  is given by [22]:

$$SL(\Omega) = 170.8 + 10 \log(\eta_{Tx} P_{elec}) + DI(\Omega) \quad [dB \text{ re } 1 \mu\text{Pa}@1m] \quad (10)$$

The term  $DI(\Omega)$  is the log-scale representation of the directivity factor ( $DI = 10\log(D_f)$ ) and the constant 170.8 captures the effect of water density, speed of sound, and reference pressure level which is  $1 \mu\text{Pa}$  in underwater acoustics. Please note that moving forward the angular dependence of  $DI$  and any derived parameters will be omitted for brevity.

**2.2.3 Acoustic propagation in the underwater channel.** The acoustic signal decays as it propagates the underwater acoustic channel over a distance  $d$  at a single frequency  $f$ , and this decay is given by the path loss ( $PL$ ) [19]:

$$PL(d, f) = k \log(d) + \alpha(f) d \quad [\text{dB}] \quad (11)$$

where  $k$  is the spreading factor (analogous to the path-loss exponent in the radio channel), and  $\alpha(f)$  is the frequency-dependant absorption coefficient in dB/m. The first term in Eq. 11 represents the spreading loss and the second term denotes the absorption loss which becomes more pronounced at higher frequencies. The spreading factor  $k$  represents the propagation geometry of the traveling wave. Specifically,  $k = 2$  denotes spherical spreading,  $k = 1$  denotes cylindrical spreading, and  $k = 1.5$  denotes practical spreading.  $\alpha(f)$  can be computed for seawater using Throp's formula given in [19]. Using the path-loss equation and the source level equation described above, we can express the received pressure level,  $RL$ , that reaches a backscatter node as:

$$RL = SL - PL \quad (12)$$

$RL$  is measured in dB re  $1 \mu\text{Pa}$  and it captures the sound intensity at a distance  $d$  meters away from Tx.

**2.2.4 From received acoustic level to harvested power.** Next, we derive the harvested electrical power from the acoustic pressure incident on the backscatter node. We consider the equivalent Z-parameter circuit shown in Fig. 2b which can be represented by the Thevenin equivalent circuit [24] shown in Fig. 2c. In this circuit,  $Z_e$  is the electrical load,  $Z_{th}$  is the Thevenin equivalent resistance, and  $V_{th}$  is the Thevenin equivalent voltage. To represent  $Z_{th}$  and  $V_{th}$  as a function of Z-parameters,  $F_b$ , and  $R_r$ , we translate port-2 (acoustic port) of Fig. 2c to port-1 (by adapting Eq. 14.4.8 of [24], where  $V_g$  and  $Z_g$  are replaced by  $F_b$  and  $R_r$ , respectively):

$$Z_{th} = Z_{in}, \quad V_{th} = \frac{Z_{12}F_b}{Z_{22} + R_r} \quad (13)$$

The harvested power on the downlink ( $P_{harv}$ ) is equivalent to the power delivered to the attached electrical load,  $Z_e$ , in Fig. 2c. Given  $V_{th}$  and  $Z_{th}$ , we can compute the power delivered to the electrical load using the following relation [24]:

$$P_{harv} = \frac{|V_{th}|^2 R_e}{|Z_e + Z_{in}|^2} \quad (14)$$

where  $R_e$  denotes the real part of  $Z_e$ . Using Eq. 13, and by simplifying, we can represent  $P_{harv}$  as:

$$P_{harv} = \frac{|F_b|^2 R_e R_{in}}{|Z_e + Z_{in}|^2 R_r} \frac{|Z_{12}|^2 R_r}{|Z_{22} + R_r|^2 R_{in}} \quad (15)$$

Notice that the second fraction in Eq. 15 is the efficiency expression that we derived in §2.2, except that the  $Z_{21}$  is replaced by  $Z_{12}$ . Assuming a passive reciprocal transducer (which is true for most underwater transducers) yields  $Z_{12} = \pm Z_{21}$ , and thus Eq. 15 simplifies to:

$$P_{harv} = \frac{|F_b|^2 \eta_{node} R_e R_{in}}{|Z_e + Z_{in}|^2 R_r} \quad (16)$$

Substituting for  $F_b$  from Eqs. 1 and 2, we obtain the following:

$$P_{harv} = \frac{\bar{F}_i^2 c D_f^{node} \eta_{node}}{\rho \pi f^2} \frac{R_e R_{in}}{|Z_e + Z_{in}|^2} \quad (17)$$

Using Eq. 12 and the definition of  $RL = 20 \log(\bar{p}_i / \bar{p}_{ref})$  [22] - where  $\bar{p}_{ref}$  is the reference pressure level ( $1 \mu\text{Pa}$ ) - we express  $P_{harv}$  in dBm (dB re 1 mW) as follows:

$$P_{harv} = 77.7 + 10 \log(\eta_{Tx} P_{elec}) + DI_{Tx} + DI_{node} + 10 \log(\eta_{node}) - 20 \log(f) - PL + IML_D \quad [\text{dBm}] \quad (18)$$

where  $DI_{node}$  is the directivity index of the node (i.e.,  $DI_{node} = 10 \log(D_f^{node})$ ), and the downlink impedance mismatch loss  $IML_D$  is defined as:

$$IML_D = 10 \log\left(\frac{R_e R_{in}}{|Z_e + Z_{in}|^2}\right) \quad (19)$$

$IML_D$  depends on the electrical impedance of the node and the connected electrical load. It achieves a max value of  $10 \log(\frac{1}{4})$  when the electrical load is conjugate matched to the node's impedance (i.e.,  $Z_e = Z_{in}^*$ ), in agreement with the maximum-power transfer theorem [24].

We can simplify Eq. 18 by defining the transduce's gain ( $G$ ) as the logarithmic sum of its efficiency and directivity:

$$G = 10 \log(\eta) + DI \quad (20)$$

By substituting Eq. 20 in Eq. 18, we arrive at a final compact expression for the downlink power:

$$P_{harv} = 77.7 + 10 \log(P_{elec}) + G_{Tx} + G_{node} - 20 \log(f) - PL + IML_D \quad [\text{dBm}] \quad (21)$$

Eq. 21 is a complete representation of all the factors that determine the downlink range of the underwater backscatter without any restriction on transducer's shape and size.

### 2.3 Uplink Channel

Our next step is to derive the uplink link-budget model and relate it to the transducer and channel parameters. We define  $BL$  as the reflected acoustic pressure level at the hydrophone due to backscatter by the node.  $BL$  can be defined following the definition of  $SL$  (Eq. 10):

$$BL = 170.8 + 10 \log(P_{refl}) + DI_{node} - PL \quad (22)$$

where  $P_{refl}$  is the reflected acoustic power from the node. The reflected power from an underwater transducer can be defined in terms of the *scattering cross-section* (SCS) which is denoted as  $\sigma$ , (the counterpart of SCS is radar cross-section (RCS) in the radio channel) as follows [25]:

$$P_{refl} = \sigma I_i \quad (23)$$

where  $I_i$  is the incident acoustic intensity and is given by [22]:

$$I_i = \frac{\tilde{P}_i^2}{\rho c} = 10^{RL/10} * \frac{\tilde{P}_{ref}^2}{\rho c} \quad (24)$$

Using Eqs. 12, 22, 23, and 24, we can express  $BL$  as:

$$BL = 159.8 + 10 \log(\eta_{Tx} P_{elec}) + DI_{Tx} + 10 \log(\sigma) + DI_{node} - 2PL \quad (25)$$

Note that the received backscatter power at the hydrophone is affected by the path loss twice which is inherent to all backscatter communication. Having defined  $BL$  as a function of  $\sigma$ , we next derive the relation between  $\sigma$  and backscatter switching (the reflection coefficient).

**2.3.1 Scattering Cross Section.** As mentioned previously, SCS relates the incident acoustic intensity and the reflected power (Eq. 23). The reflected power  $P_{refl}$ , in turn, is a function of the acoustic power absorbed by the node  $P_{absorb}$  and the maximum available power at the node.  $P_{absorb}$  is defined in terms of transducer parameters as [24]:

$$P_{absorb} = \frac{|F_b|^2 R_r}{|R_r + Z_o|^2} \quad (26)$$

According to the maximum-power transfer theorem, the available power at the node is maximized when  $Z_o$  is conjugate matched to  $R_r$  (i.e.,  $Z_o = R_r$ ). In this case, the maximum available power,  $P_{avail}$ , is given by [24]:

$$P_{avail} = \frac{|F_b|^2}{4R_r} \quad (27)$$

While  $P_{refl}$  is related to  $P_{avail}$  by [24]:

$$P_{refl} = |\Gamma|^2 P_{avail} = \frac{|\Gamma|^2 |F_b|^2}{4R_r} \quad (28)$$

where  $\Gamma$  is the acoustic reflection coefficient, and it is defined in terms of the transducer equivalent acoustic impedance  $Z_o$  and its radiation resistance  $R_r$  by [24]:

$$|\Gamma| = \left| \frac{R_r - Z_o^*}{R_r + Z_o} \right| \quad (29)$$

Using Eqs. 1, 2, 23, 24, 28, and the facts that  $w = 2\pi f$  and  $\lambda = \frac{c}{f}$ , we derive SCS as a function of  $\Gamma$ :

$$\sigma = \frac{\lambda^2 D_f^{node} |\Gamma|^2}{4\pi} \quad (30)$$

where  $\lambda$  is the wavelength of the traveling acoustic waves. As the backscatter node communicates via switching between two states, its reflection coefficient also toggles between two states, and this results in a differential scattering cross-section ( $\Delta\sigma$ ) which is expressed as:

$$\boxed{\Delta\sigma = \frac{\lambda^2 D_f^{node} |\Delta\Gamma|^2}{4\pi}} \quad (31)$$

It is worth mentioning here that the expression for underwater backscatter differential SCS is similar to the differential RCS for RF backscatter, indicating that the governing physical principles of backscatter communication are the same

in both mediums. Using the derived relationship of  $\Delta\sigma$  and Eq. 25, we express  $BL$  as a function of  $\Delta\Gamma$ :

$$BL = 159.8 + 10 \log(\eta_{Tx} P_{elec}) + DI_{Tx} + 10 \log\left(\frac{\lambda^2 |\Delta\Gamma|^2}{4\pi}\right) + 2DI_{node} - 2PL \quad (32)$$

**2.3.2 Breaking down Reflection Coefficient.** We next relate  $\Delta\Gamma$  to the backscatter node properties using Z-parameters (discussed in Sec. 2.1.1) and circuit theory. We start by expressing the transducer's acoustic impedance,  $Z_o$  in terms of Z-parameters [24]:

$$Z_o = Z_{22} - \frac{Z_{12}Z_{21}}{Z_{11} + Z_e} \quad (33)$$

Next, we eliminate the term  $Z_{11}$  by substituting for it in terms of the easily measurable electrical impedance  $Z_{in}$  using Eq. 6:

$$Z_o = Z_{22} - \frac{Z_{12}Z_{21}}{Z_{in} + Z_e + \frac{Z_{12}Z_{21}}{Z_{22} + R_r}} \quad (34)$$

Substituting into Eqs. 29, and assuming a reciprocal transducer (i.e.,  $Z_{12} = Z_{21}$ ), yields:

$$\Gamma = \frac{(Z_{22}^2 - R_r^2)(Z_{in} + Z_e) - 2R_r Z_{21}^2}{(Z_{22} + R_r)^2 (Z_{in} + Z_e)} \quad (35)$$

Since we modulate between two impedance states ( $Z_{e1}, Z_{e2}$ ), the differential reflection coefficient simplifies to:

$$|\Delta\Gamma| = 2\eta_{node} R_{in} \left( \frac{|Z_{e2} - Z_{e1}|}{|Z_{in} + Z_{e1}| |Z_{in} + Z_{e2}|} \right) \quad (36)$$

where we used the expression for the electromechanical efficiency in Eq. 9 to simplify the expression above. Substituting by Eq. 36 into Eq. 32 yields an expression for  $BL$  in terms of measurable transducer parameters:

$$BL = 159.8 + 10 \log(\eta_{Tx} P_{elec}) + DI_{Tx} + 10 \log\left(\frac{\eta_{node}^2 \lambda^2}{\pi}\right) + 2DI_{node} - 2PL + IML_U \quad (37)$$

where

$$IML_U = 20 \log \left( R_{in} \left( \frac{|Z_{e2} - Z_{e1}|}{|Z_{in} + Z_{e1}| |Z_{in} + Z_{e2}|} \right) \right) \quad (38)$$

represents the logarithmic loss due to impedance mismatch. This loss can be practically calculated by measuring the electrical impedance of the backscatter transducer, and the switched electrical load separately. Note that switching the electrical impedance between open and matched load ( $Z_{e1} = \infty$  and  $Z_{e2} = -X_{in}$ , where  $X_{in}$  is the imaginary part of  $Z_{in}$ ) results in the maximum differential reflection:

$$\boxed{|\Delta\Gamma|_{max} = 2\eta_{node}} \quad (39)$$

The equation above suggests that if the transducer is electrically matched, the reflected power is only limited by the transducer's efficiency.

By substituting Eq. 20 in Eq. 37, we can simplify  $BL$  to:

$$\boxed{BL = 159.8 + 10 \log(P_{elec}) + G_{Tx} + 10 \log\left(\frac{\lambda^2}{\pi}\right) + 2G_{node} - 2PL + IML_U} \quad (40)$$

Eq. 40 defines backscatter level in terms of transducers' gain and impedance which are easily quantifiable (experimentally and numerically). It accounts for transducer properties and captures all the electrical, mechanical, and acoustic factors contributing to backscatter.

While the above analysis focused on piezoelectric transducers, the derived model for the backscatter channel is applicable to electromagnetic transducers (e.g., moving-coil and magnetostrictive transducers). Electromagnetic transducers have an antisymmetric Z-matrix ( $Z_{12} = -Z_{21}$ ) (unlike symmetry in piezoelectric transducers  $Z_{12} = Z_{21}$ ). Interestingly, this would not change our final expressions (i.e., Eq. 21 and 40) because this anti-symmetry would only cause a sign change in an intermediate equation (Eq. 29) which cancels out in the final derivation.

## 2.4 Extending Backscatter level to SNR

Finally, we derive the *SNR* from the *BL* (signal power) by incorporating underwater noise. Prior work has extensively studied ambient noise in the ocean as a function of four main sources: shipping activities, thermal noise, water waves, and turbulence [26]. The combination of these noise sources, *NL*, represents the power spectral density of the noise and we can use it to compute the *SNR* [19]:

$$SNR = BL - (NL + 10 \log(BW)) \quad (41)$$

where *BW* represents the signal's bandwidth. We note that depending on sea conditions, the ambient noise can vary between  $25 - 55$  dB re  $1\mu Pa^2/Hz$  in the frequency range of 10-20 kHz [22]. In the case of rivers and lakes, depending on the shipping/boating activities, the noise can exceed 80 dB re  $1\mu Pa^2/Hz$  in the 10-20 kHz band depending on the proximity of the activity and its nature [27, 28].

## 2.5 How to Use the Link Budget

So far, we have derived the analytical expressions for the link budget. Next, we describe how engineers can use these expressions in modeling and designing backscatter systems.

The key link budget equations for system design are Eq. 21, Eq. 40, and Eq. 41. To use these in practice, an engineer needs to plug in the values for their different parameters. We differentiate between three types of parameters. The first is determined by design; it includes the frequency (*f*), wavelength ( $\lambda$ ), electrical power ( $P_{elec}$ ), and bandwidth (*BW*). The second set of parameters are those of the channel, specifically path loss (*PL*) and noise level (*NL*); these can be obtained from models in past literature [19]. The third set of parameters needs to be derived from the transducer datasheets (or through experimentation). It includes the gain  $G_{Tx}$  and  $G_{node}$ ; it also includes  $IMD_D$  and  $IMD_U$ , which are functions of the electrical impedances *Z* and resistances *R*. While *Z* and *R* are commonly reported in transducer datasheets [29–31] (or can be experimentally obtained using an impedance analyzer), the transducer's gain *G* is not commonly provided.

To obtain *G*, one can calculate it from Eq. 20 when the transducer's *DI* and  $\eta$  are reported separately in the datasheet which is seldom the case.<sup>4</sup> Instead, transducer manufacturers commonly report the transmit voltage response (*TVR*) which relates the generated acoustic pressure in one direction to the applied electrical voltage [29–31]. Fortunately, *G* (which relates the acoustic intensity in one direction to the input electrical power) can be calculated from *TVR* using:

$$G = TVR - 10 \log(\text{real}(1/Z)) - 170.8 \quad (42)$$

The parameters *TVR* and *Z* (commonly reported in transducers datasheets) are thus sufficient to fully evaluate our up-link/downlink budget models. Alternatively, a transducer's *TVR* can be experimentally characterized using a calibrated hydrophone placed 1 m from the transducer using standard transducer calibration procedures [32].

## 3 NUMERICAL VALIDATION

We assess the validity of the analytical expressions for the harvested power  $P_{harv}$  (Eq. 21) and the backscatter level *BL* (Eq. 40) in two phases. First, we apply the models to spherical shell piezoelectric transducers which are the simplest form of underwater transducers, and the only type of underwater transducers with closed-form expressions for all their acoustic parameters. However, spherical transducers are omnidirectional regardless of their operating frequency, so this analysis only validates a special case of our analytical expression with *DI* = 0. Second, we extend our analysis to potted cylindrical transducers with a directional radiation pattern that depends on frequency, but does not have closed-form analytical expressions for most of its acoustic parameters at practical backscatter frequencies. This is a more general case that applies to most underwater transducers used in practice.

### 3.1 Ideal Spherical Transducers

In this section, we first describe an equivalent circuit model for spherical transducers which will be used to evaluate acoustic backscatter metrics (*BL* and  $P_{harv}$ ) in closed-form. Then, we present a high-fidelity multiphysics finite-element model (FEM) for a complete acoustic backscatter system and use this model to validate the analytical results.

**3.1.1 Closed-Form Analytical model.** The equivalent circuit parameters (shown in Fig. 2a) for spherical shell transducers are well-known and can be found in [22] as a function of transducer geometry and material properties. We used the equivalent circuit model (Fig. 2a) to evaluate the impedance matrix representation for a spherical transducer and to calculate analytical backscatter as detailed in §2.2 and §2.3.

**3.1.2 Modeling backscatter numerically.** To validate the analytical backscatter, we build a high-fidelity numerical

<sup>4</sup>Empirically measuring a transducer's efficiency or directivity separately requires a 2-axis rotational setup to measure the acoustic power generated by the transducer in all directions which is prone to experimental errors.

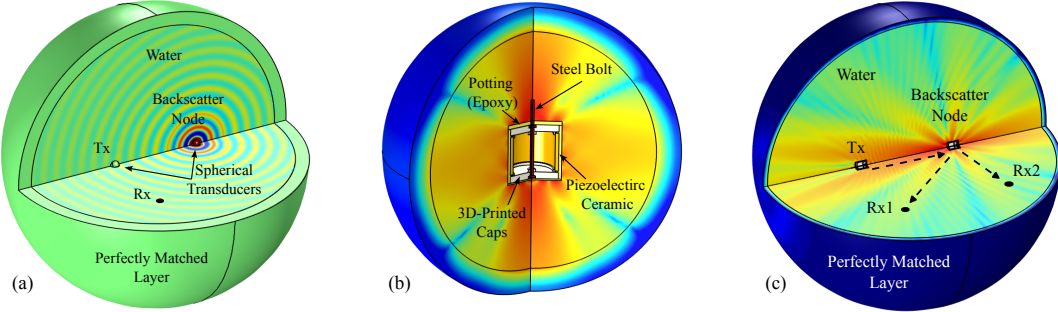


**Figure 3: Numerical Simulations.** (a) The backscattered pressure from a spherical transducer. Positive pressure is in red and negative pressure in blue. (b) A model for characterizing cylindrical transducers. The heatmap shows the sound level generated by the transducer at 30 kHz (red indicates higher sound level). (c) The backscatter level from a cylindrical transducer at 40 kHz. Black arrows highlight acoustic propagation from Tx to two receiver locations Rx1 and Rx2.

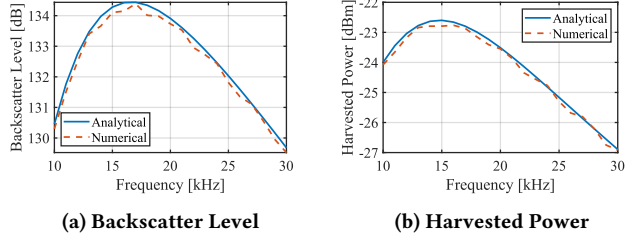


**Figure 4: Numerical validation for spherical transducers.** shows the Analytical (blue) and numerical (red) (a) backscatter levels and b harvested power for two spherical transducers separated by 0.5 m as observed by a hydrophone 0.5 m away from the backscatter node.

model of backscatter in COMSOL Multiphysics [21]. The model, shown in Fig. 3a, is an electro-piezo-acoustic FEM simulation in the frequency domain. It models Tx (including the driving electrical circuit), backscatter node (including load circuit), and acoustic propagation in an infinite underwater domain. The system is simulated as a 2D axisymmetric model to reduce computational resources and solution time.

**3.1.3 Numerical model implementation.** The system comprises two piezoelectric spherical shell transducers (2.5 cm in diameter and 0.5 mm in thickness) in a large spherical acoustic domain as shown in Fig. 3a. The transducers material is PZT-4 which is a common material in underwater piezoelectric transducers. Tx is driven by a voltage source of amplitude 1 V, while the backscatter node is connected to a variable resistor. The transducer separation distance is kept small (50 cm) to reduce the number of degrees of freedom in the model, since the model complexity (size, memory, and solution time) scales with the square of the distance. The acoustic domain is discretized with a minimum of five elements per wavelength [21]. Perfectly matched layers (PMLs) are used at the acoustic domain boundaries to simulate an infinite domain. Acoustic backscatter is calculated by running the simulation twice with a different electrical resistor to emulate electrical switching. The backscattered pressure field (shown in Fig. 3a) is the difference between the steady state pressure fields calculated from each simulation  $BL = 20 \log ((\bar{p}_1 - \bar{p}_2)/\bar{p}_{ref})$ .

**3.1.4 Spherical Transducers Results.** Fig. 4a compares analytical  $BL$  (solid blue) to numerical predictions from FEM (dashed red) for the backscatter system shown in Fig. 3a. The backscatter level is normalized by the input electrical power at Tx (e.g. assuming a uniform 1 W of input electrical power at each frequency). The results shown are reported for an Rx located 50 cm away from Tx (Fig. 3a), and for switching between two arbitrary resistors with values 1  $\Omega$  and 100  $\Omega$ . We note:

- The analytical and numerical results are in excellent agreement throughout the simulated frequency range, with a median deviation of 0.17 dB.
- The analytical model slightly overpredicts  $BL$  since it adopts the thin shell approximation which neglects the transducer's radial stresses.
- The backscatter level peaks near 16 kHz which is slightly lower than the water-loaded transducer resonance.

Fig. 4b shows the harvested electrical power by the backscatter node in dBm when 1 W of power is fed to Tx and a 100  $\Omega$  resistor is connected to the backscatter node. The plot shows the analytical predictions (solid blue) and the numerical results (dashed red) as a function of frequency. We note:

- The analytical and numerical results are in excellent agreement for the entire frequency range.
- The harvested power peaks at 15 kHz which is lower than the  $BL$  peak, and is mainly determined by the impedance loss factor (Eq. 19) between the load resistor (100  $\Omega$ ) and the backscatter node's electrical impedance.

Fig. 4a and Fig. 4b demonstrate the validity of the analytical models for the special case of idealized omnidirectional spherical transducers. The modeling and analysis of practical, directive backscatter transducer is discussed next.

### 3.2 Practical Transducers

Encapsulated (potted) cylindrical transducers were used in previous underwater acoustic backscatter implementations [12, 13], but similar to most practical transducers, they do not have a closed-form analytical expression. In this section, we develop a semi-analytical approach to predict the backscatter performance of practical transducers, and validate this

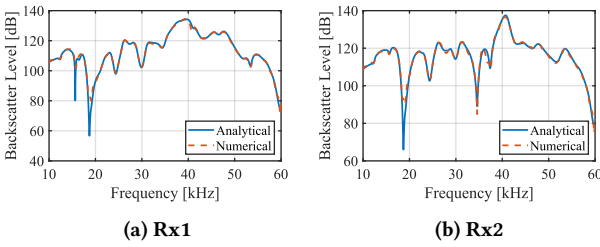


**Figure 5: Backscatter Level vs Frequency.** Analytical backscatter level (solid blue) compared to numerical results (dashed red) for two encapsulated cylindrical transducers separated by 0.5 m as observed by hydrophones (a) Rx1 and (b) Rx2 whose locations are shown in Fig. 3c.

approach by comparing its predictions to pure numerical models for calculating backscatter.

**3.2.1 Analytical Model.** Cylindrical transducers with moderate aspect ratios are difficult to model analytically for practical frequencies, especially, when the fully potted (encapsulated for electrical insulation and waterproofing) transducer is considered. Instead, we extract the transducer parameters numerically using a FEM simulation. To extract transducer parameters, we simulate a single transducer placed in an infinite acoustic domain, as shown in Fig. 3b. Only  $G$  and  $Z_{in}$  are required to fully characterize a piezoelectric transducer according to Eqs. 21&40. To calculate  $G$  and  $Z_{in}$ , we excite the transducer with a voltage  $V_{in}$ , and calculate the acoustic pressure 1 m away from the transducer (in the far field)  $\bar{p}_{out}$ . The transducer gain is then calculated as:

$$G(f, \Omega) = 20 \log \left( \frac{\bar{p}_{out}(f, \Omega)}{\bar{p}_{ref}} \right) - 170.8 - 10 \log(P_{in}) \quad (43)$$

where  $P_{in} = \frac{1}{2} re(V_{in} I_{in}^*)$  is the input electrical power to the transducer,  $I_{in}^*$  is the complex conjugate of the input current, and  $\Omega$  is the angle at which the pressure is measured. We calculate the transducer's electrical impedance from  $Z_{in} = V_{in}/I_{in}$  and, finally, use Eq. 40 to find the analytical BL.

**3.2.2 Numerical Model.** We calculate acoustic backscatter numerically for the cylindrical transducers using the FEM model shown in Fig. 3c. We follow the same procedure used to construct the FEM in the previous section. The transducers are oriented such that the bottom caps are facing each other, so that the model is axisymmetric, avoiding a resource-intensive full-3D model. The backscatter level is calculated using the differential pressure at multiple locations to assess the influence of directivity on the results.

**3.2.3 Practical Transducer Results.** We investigate the ability of our analytical expression to predict acoustic backscatter in different directions. Fig. 5 compares the analytical and numerical results for backscatter from a practical directional transducer. As shown in Fig. 3c, the backscattered field from a cylindrical transducer is complex and directional at frequencies higher than its fundamental resonance ( $\sim 17$  kHz). Thus, we present the results for two different receivers (Rx1

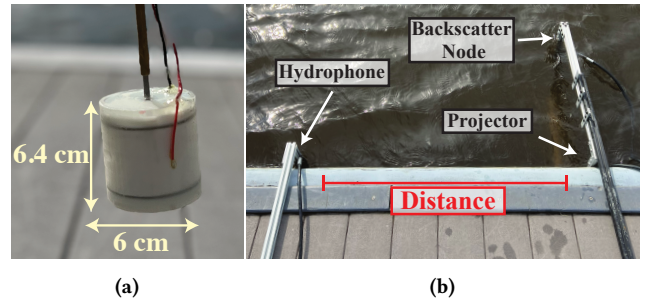


**Figure 6: Experimental Setup:** (a) shows our in-house backscatter node. (b) shows an experimental setup including the projector (Tx), backscatter node and hydrophone (Rx) locations.

in Fig. 5a and Rx2 in Fig. 5b), and their locations are indicated in Fig. 3c. We make the following remarks on Fig. 5:

- The analytical and numerical predictions match extremely well for both directions (median error less than 0.4 dBm), suggesting that our analytical expressions can be applied to predict backscatter in multiple directions.
- The plots show large variability in the backscattered level versus the operation frequency and Rx location, suggesting that backscatter needs to be evaluated versus angle for directional nodes to select optimum operating frequency based on Rx location and node orientation.
- The plots show that backscatter peaks for both locations around 40 kHz suggesting that it is a favorable operating frequency when the transducers are oriented with the end-caps facing each other.<sup>5</sup>
- The numerical and analytical results deviate at the valleys (transducer nulls) for both directions because of minute reflections from acoustic domain boundaries. Using PML layers reduces such reflections significantly, but it does not eliminate them causing a mismatch with the analytical predictions which assumes an infinite acoustic domain.

## 4 EXPERIMENTAL VALIDATION

To experimentally validate the analytical model, we implemented and evaluated an underwater backscatter system.

### 4.1 Implementation

Our implementation consists of three components: (1) Piezo-acoustic backscatter nodes, similar to the one shown in Fig 6a. We fabricated these nodes in-house following similar procedures to past work [12, 13] using the SMC5447T4011 piezo-ceramic [33], whose nominal frequency is 17 kHz. (2) An in-house fabricated Tx (similar to the node) connected to a Crown XLI 3500 audio amplifier [34], which is in turn connected to an N210 USRP [35] software radio to generate the downlink signal. (3) A receiver consisting of an omnidirectional Reson TC4014 hydrophone [36] which has a differential receive voltage sensitivity of  $-180$  dB re  $1V/\mu\text{Pa}$ . The

<sup>5</sup>Recall that we oriented the transducers toward each other here to avoid a resource-intensive simulation required for modeling lateral placements.

output of the hydrophone is fed to a 4-channel Rigol HDO 1074 oscilloscope [37] via a differential voltage probe [38]. The oscilloscope is controlled through a LabVIEW code to record the experimental data. In addition to recording the hydrophone output, the oscilloscope simultaneously records Tx voltage to calculate the input electrical power. Similarly, the oscilloscope measures the voltage at the backscatter node during downlink power harvesting verification experiments. Processing is performed offline in MATLAB.

## 4.2 Experimental setup

We performed the verification experiments in a river (4 meters deep) at different locations. An example setup of one of our experiments is shown in Fig. 6b. To make our setup rigid against underwater currents, we attach our projector, hydrophone, and the backscatter node to 2-meter-long 80-20 aluminum rods. Since the evaluation environment was shallow, we conducted the experiments at close distances ( $\sim$ 1-3 meters) to minimize multipath.

**4.2.1 Gain measurement.** We characterized the gain of Tx and the backscatter node by exciting each node with a voltage pulse and measuring the sound pressure level 1 m away from the node. For each node, we generate a series of Gaussian pulses with 2 kHz bandwidth and sweep the center frequency between 10 kHz and 18 kHz. The Oscilloscope is triggered at the start of each excitation pulse, and a total of 64 measurements are averaged for each frequency to reduce random noise. We record 4 ms time series of the input voltage and the output hydrophone pressure signal. We then time-gate them to eliminate echoes. The signals are summed and converted to the frequency domain via FFT, and the node gain is calculated for the frequencies of interest using Eq. 43.

**4.2.2 Downlink Power.** To experimentally verify the harvested power, we terminate our backscatter node to a resistive load ( $56 \Omega$ ) and a parallel inductor of 1.5 mH, acting as a narrowband matching network, and measure the voltage across the resistor using a differential probe and an oscilloscope (as discussed in §4.2). Tx sends a Gaussian pulse sweep from 10 - 18 kHz and we record the resultant signal across the resistor and the input voltage signal to Tx. We use an impedance analyzer [39] to measure the electrical impedance (as a function of frequency) of the node, Tx, and the matching network to compute the harvested power, input electrical power, and the impedance mismatch loss, respectively.

**4.2.3 Measuring Backscatter Level.** To measure  $BL$ , the Tx linearly sweeps a sinusoidal frequency from 10 kHz to 18 kHz in steps of 100 Hz. Each frequency is transmitted for 500 ms followed by a pause of 100 ms. On the backscatter side, we use a signal generator and N-channel MOSFETs to generate an ON-OFF switching signal of 500 Hz. The node is switched between short-circuit and a narrow-band transformer-based matching network. For the transformer core, we use an RM-6

ferrite core with  $A_L = 250 \text{ nH}$  [40], providing 250 nH per turn squared. Similar to the downlink power experiments, we use the impedance analyzer to measure the impedance of the backscatter node and the transformer (both in open and short states) to compute the impedance mismatch loss (described in §2.3.1). The scope samples hydrophone signal at a sampling rate of 200 kHz. To compute  $BL$  (i.e., backscatter signal power) at each frequency, we take an FFT of the hydrophone data in Matlab and sample the fundamental harmonics of the backscatter switching signal which appears on either side of the carrier at a frequency offset of 500 Hz (i.e., a carrier with frequency  $f_c$  will have switching harmonics at  $f_c + 500 \text{ Hz}$  and at  $f_c - 500 \text{ Hz}$ ). We then use Parseval's theorem [41] to compute the power of the signal.

## 4.3 Experimental vs Analytical Results

**4.3.1 Harvested power vs Frequency.** We used the experimental setup and procedure described above to verify the downlink expression (Eq. 21) experimentally. In this experiment, we arranged the Tx, Rx and the node in an equilateral setup (using 80-20 rods) with 60 cm between each two transducers. We measure the gain of Tx and the node using the procedure detailed in §4.2. We normalize the measured harvested power at each frequency by the transmitted power at that frequency to remove the effect of impedance mismatch at Tx. Using the measured gain and impedance values we compute the analytical downlink power using Eq. 21. Our analytical model assumes spherical spreading for path loss computation. Fig. 7a plots the harvested power in dBm against frequency for the analytical model (solid blue) and experimental measurements (dotted red). We note:

- The harvested power predicted by the model accurately tracks the experimentally measured power. The error between the model and experimental curves remain within 1-2 dB across a large range of frequencies, and the median deviation across frequencies is 1.5 dB.
- Both model and measurement suggest that for these transducers, the 15 kHz neighborhood is an optimal region of operation as the harvested power peaks to -15 dBm. Both analytical and experimental results show a null around 17 kHz suggesting a performance degradation around this region.
- The experimental and analytical measurements deviate by more than 10 dB around the valley (17 kHz). This is likely due to errors in measurements that occur at much lower harvested power (where the measurement instruments become more susceptible to noise).

These results show that our analytical model for downlink harvested power is accurate and it captures all the components of the system that determine downlink performance.

**4.3.2 Backscatter level vs Frequency.** Next, we experimentally verify the end-to-end link budget model by comparing

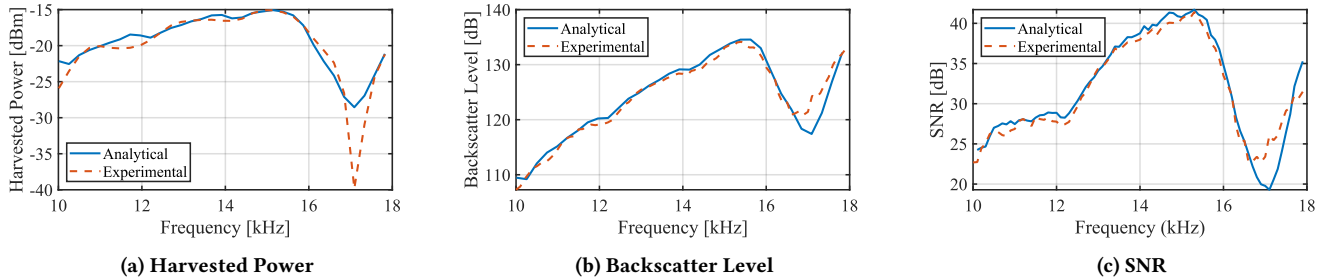


**Figure 7: Experimental Verification.** (a) plots the harvested power vs frequency on the downlink for the analytical model (solid blue) and experimental measurements (dotted red). (b) plots the Backscatter Level as a function of frequency for the analytical model (solid blue) and experimental measurements (dotted red). (c) plots the SNR against the frequency for the analytical model (solid blue) and experimental measurements (dotted red).

the analytical and experimental backscatter levels. Similar to the downlink verification experiments, we measure the gains, and impedance values to compute the uplink analytical  $BL$  (using Eq. 40) then compare it against the normalized experimental  $BL$ . Fig. 7b plots the analytical backscatter level (solid blue) and the experimental backscatter level (dotted red) as a function of frequency. We note:

- Analytical backscatter level curve accurately tracks the experimental values across frequencies, and both curves remain within 1 dB of each other across a large range of frequencies with a median deviation of 0.76 dB (which is well within the hydrophone’s precision of 3 dB [36]).
- Our theoretical model and experimental measurements show that the backscatter level increases linearly with frequencies from 110 dB at 10 kHz to its peak value of 135 dB at 15.5 kHz. This suggests that the region around 15 kHz is suitable for the backscatter setup’s operation. Similar to the experimental results of downlink harvested power, the backscatter level results also show that there is a null in the transducers’ response around 17 kHz.

This experimental validation suggests that our end-to-end link budget model accurately captures the performance of underwater backscatter across frequencies.

**4.3.3 SNR vs Frequency.** Finally, we validate the analytical uplink SNR against the experimental measurements across the frequency range of 10–18 kHz. We estimate the experimental SNR by computing the received signal power and the noise power in our experimental environment. We compute the signal power (i.e., backscatter level) across frequencies using the same method described above, and we quantify the noise using the hydrophone signal in the absence of backscatter, but with Tx turned on. Measuring the noise with Tx on allows us to capture the impact of self-interference noise [13] (in addition to the ambient noise) in the band of interest. Since we measure signal power across frequencies, we also record experimental noise across frequencies by linearly sweeping the carrier frequency of Tx (similar to how we measure backscatter level). We then use the power-spectral density (p.s.d) of the measured noise [42] to compute noise

power in the band of interest. We compute the SNR by subtracting the measured noise power from the signal power in dBs. We use the same measured noise in the analytical model to compute analytical SNR.

Fig. 7c plots the analytical (solid blue) and experimental SNR (dotted red) vs frequency. We note the following:

- Analytical SNR and measured SNR curves match well across frequencies, with a median deviation of only 0.75 dB.
- Both curves show that SNR increases monotonically from ~25 dB at 10 kHz to a peak value of 40 dB around 15 kHz and then it sharply dips below 25 dB around 17 kHz. We expect this result because our initial experiments of backscatter level measurements suggest that the backscatter response has a null around 17 kHz.
- The SNR is quite high in this experiment (between 20–40 dB) because the backscatter node is relatively close to the Tx and Rx. Recall that this was done to minimize the impact of multipath on the model. We note that we intentionally avoided incorporating multipath into the analytical model since it does not contribute to advancing our understanding of the underwater link budget.<sup>6</sup>

This SNR result validates our end-to-end analytical model and it shows that the model can accurately capture the backscatter performance across frequencies.

## 5 EXTENDED ANALYSIS

Now that we have validated our model through simulations and experiments, we use this model to analyze the backscatter performance as a function of different system parameters.

### 5.1 Input Electrical Power

First, we study the impact of input electrical power on the uplink communication range. For this result, we use the experimentally characterized parameters (i.e., gains and operational frequency) of our in-house fabricated transducers. We use 15 kHz as the carrier frequency since our experimental

<sup>6</sup>While multipath is important for equalization, decoders, and localization technologies, it is largely orthogonal to the contributions of this work and can be incorporated by replacing the  $PL$  term with the appropriate fading terms for the corresponding medium.

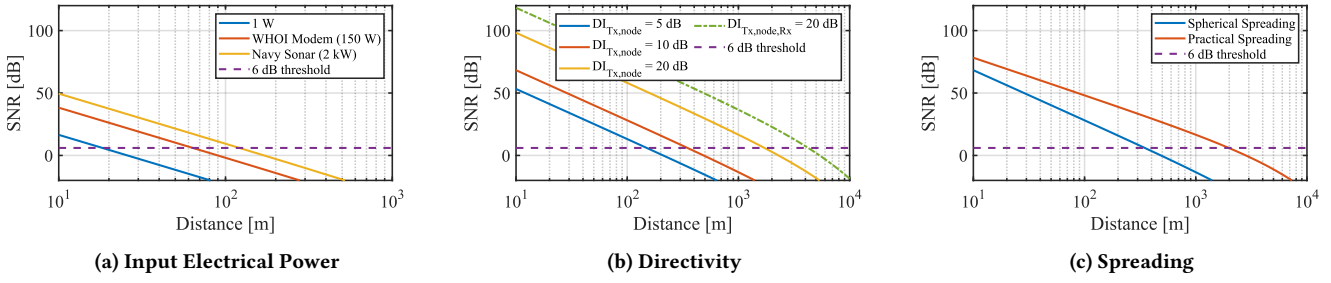


**Figure 8: Theoretical Uplink Communication Range:** (a) plots SNR vs distance for our in-house transducers while varying the input electrical power between 1 W (blue), 150 W (red), and 2 kW (yellow). (b) plots the SNR vs distance for a transmit power of 150 W and a Tx/node directivity index of 5 dB (blue), 10 dB (red), and 20 dB (yellow) and Tx/node/Rx directivity of 20 dB (green). (c) plots SNR vs distance for two different spreading factors. The red curve plots the practical spreading ( $k = 1.5$ ) and the blue curve plots the spherical spreading ( $k = 1.5$ ). The dashed line shows the 6 dB decoding threshold.

results (per §4.3) suggested it is the optimal operating point for these transducers. We assume perfect impedance matching,<sup>7</sup> spherical spreading ( $k = 2$ ), a bandwidth of 500 Hz (which is typical in underwater acoustic communications), and we use standard ocean noise models (described in §2.4) with a windspeed of 10 m/s and a moderate shipping activity ( $s = 0.5$ ). We use three different power levels: 1 W, 150 Watt which is the standard power consumption of the WHOI low-power micromodem [43], and 2 kW used by the Navy in active sonar [44]. We used 6 dB as a decoding threshold [12].

Fig. 8a plots the uplink SNR against the distance for input power of 1 W (blue), 150 W (red), and 2 kW (yellow). The figure shows that the SNR drops below the decodable threshold (6 dB) for 1 W of input power around 20 meters. Increasing the power to 150 W results in increasing the decodable range to roughly 60 meters, and it further increases beyond 100 meters with 2 kW of input electrical power. These results show that even with standard low-power acoustics (i.e., WHOI micro-modems), 60 m of range is possible using our unoptimized setup, and may be further extended through coding gain (at lower throughputs).

## 5.2 Impact of Directivity

Next, we study the impact of directivity on range performance. We assume the same parameters as the previous simulation, fix the input electrical power to 150 W (similar to the WHOI low-power micro-modem), and vary directivity. We use three directivity values 5 dB, 10 dB, and 20 dB based on existing commercial transducers [45].

Fig. 8b plots the uplink SNR vs distance for three directivity values for Tx and the node: 5 dB (blue), 10 dB (red), and 20 dB (yellow) with an omnidirectional receiver, as well as a case where Tx, Rx, and node have 20 dB directivity (dotted green). The plot shows that for a DI of 5 dB, the uplink SNR is decodable (above 6 dB) up to 150 meters, and with 10 dB, it is decodable up to 350 meters. The 20 dB DI transducers push the uplink decoding range up to several kilometers. Note that

<sup>7</sup>Our practical matching was within 96% (leading to less than 0.5 dB of loss), which suggests that perfect electrical matching is a reasonable assumption at these bandwidths.

the green curve bends at higher ranges because the effect of absorption loss (sec. §2.2.3) becomes more pronounced at greater distances. These results show that directive transducers can extend the operation range of the underwater backscatter to enable real-world applications.

## 5.3 Spreading Loss

Finally, we study the impact of the spreading factor on the achievable range to understand the backscatter performance in different environments. Specifically, the decay experienced by a traveling acoustic wave depends on the depth and sound speed profile of the water column (e.g. shallow water vs a vertical link in the ocean) [46]. We use the same parameters described earlier with ( $DI_{Tx,node} = 10$  dB,  $P_{elec} = 150$  W, and  $DI_{Rx} = 0$  dB) and evaluate two values for spreading factors: 1.5 (practical spreading in shallow waters and sound channels [19]) and 2 (spherical spreading).

Fig. 8c plots the effect of spreading on the uplink performance. The blue curve represents spherical spreading and the red curve shows practical spreading. We note that the uplink SNR is decodable for distances greater than 300 meters for environments with spherical spreading. In comparison, the uplink range increases to more than a kilometer in an environment with practical spreading. These results show the influence of the operation environment on the performance of a backscatter system and highlight the extended ranges achievable in underwater environments which guide acoustic propagation.

## 6 RELATED WORK

### 6.1 Backscatter in other media

The majority of past work on backscatter link budget has focused on RF backscatter in air, e.g., RFIDs [16, 17, 20, 47]. Past work has also looked into modeling backscatter in metal and concrete [48–50] and in ultrasound inside the body [51–53]. Our work builds on this past literature and is the first to bring such analysis to the underwater domain, addressing unique properties such as differential SCS, piezoelectric properties, and acoustic propagation in water. Past work on ultrasound inside the body and metals differs from our analysis due to

the near-field nature of their operation, resulting in fundamental differences in both transducer behavior (coupling) and propagation characteristics (near vs far-field).

## 6.2 Underwater acoustics

Underwater acoustics is a well-developed field, and past work has modeled the underwater communication channel [18, 19], acoustic propagation [46, 54], and energy harvesting [14, 55, 56]. Our model builds on this past work and incorporates it into our link budget, extending it with parameters that have not been part of traditional underwater communication systems (e.g., differential SCS). Recent work has developed a preliminary underwater backscatter link budget [14, 57] but ignored the most critical component of backscatter, namely differential SCS, and was limited to analytical modeling. Our research builds on this past literature by introducing the first comprehensive end-to-end model for underwater backscatter and verifying it through both physics-based simulations and real-world empirical evaluation.

## 6.3 Underwater transducer modeling

Piezoelectric transducers are modeled in a variety of approaches depending on their operating frequencies with equivalent circuit (lumped-parameter) models used for low frequency transducers [22, 58] (below 100 kHz), and transmission line models (matrix-based) models used for high frequency transducers [59] (above 500kHz). Numerical methods (such as FEM and the boundary-element method BEM) are also popular for practical transducer design, characterization, and parameter identification [23]. Some past work has also studied scattering and reflection of underwater structures including standard transducer geometries [60, 61], but not of backscatter modulation. This work builds on existing transducer models to develop analytical expressions for electro-acoustic reflection from piezoelectric transducers regardless of the modeling approach and operating frequency. Our model defines the first generalized expression of the electromechanical SCS in terms of fundamental properties of piezoelectric transducers with no restriction on transducer geometry or modeling approach.

## 7 DISCUSSION & EXTENSIONS

This paper presented the first closed-form analytical model for underwater backscatter and verified it through numerical simulations and real-world experiments. This model informs future work in multiple directions:

**Complex Channels:** The paper focused on the fundamental link budget, which is independent of specific parameters of the underwater channel, modulation, or sensing technique. Since these parameters are common between backscatter and traditional underwater acoustic communications, the model can be extended with such parameters from the well-established literature on underwater acoustic channels. In particular, future work can extend our model to channels

with multipath, thermoclines, and complex noise by leveraging methods like Bellhop ray-tracing, ocean current simulations, and statistical models.

**Communication Parameters:** Our analysis focused on an active downlink source, FM0 modulation, and ambient noise. It would be interesting to extend this analysis to higher-order modulations, analog backscatter, and ambient underwater backscatter as well as unpacking the self-interference noise.

**Longer-Range Backscatter:** This work informs the design of next-generation underwater backscatter systems. In particular, our analysis enables understanding the performance of these systems as a function of design decisions and constraints such as power level, bandwidth/throughput, directivity, etc. The performance analysis framework shows that by applying coding, one could further lower the 6-dB threshold and operate over longer ranges (at the expense of lower throughput). Similarly, by enhancing directivity via sophisticated transducers, arraying, or using other networking architectures like multihop, one could achieve longer communication ranges.

**Marine Mammal Protection:** This work provides a critical tool - that outlines practical and measurable component specifications - for engineers to quantify the sound levels and optimize their designs. This tool can be used to design systems that emit safe sound levels for marine mammals and comply with the Marine Mammal Protection Act [62].

## 8 CONCLUSION

This paper marks an important step in our understanding of underwater backscatter and informs future research toward a new generation of underwater networks. Our results show that underwater backscatter systems can achieve several kilometers of communication range, making them viable for near-shore (coastal) monitoring of environmental hazards, hurricanes, tsunamis, aquaculture farms, and medium/short-range navigation. Future work that extends the communication range to tens of kilometers would open up even more possibilities in deep-sea exploration, under-ice navigation, and deep-ocean monitoring.

As this field evolves, this model can evolve with it to continue informing the development of newer generations of these systems, similar to how modeling cellular networks has enabled advancing them toward 6G. As underwater backscatter systems evolve, they can help contribute to various applications including underwater climate change monitoring, weather prediction, seafood production, disaster response, and more.

**Acknowledgments.** We thank our shepherd, the anonymous reviewers, and the Signal Kinetics group for their feedback. The research is funded by the Office of Naval Research, Sloan Research Fellowship, National Science Foundation, MIT Media Lab, and Doherty Chair in Ocean Utilization.

## REFERENCES

- [1] Camilo Mora, Derek P Tittensor, Sina Adl, Alastair GB Simpson, and Boris Worm. How many species are there on earth and in the ocean? *PLoS biology*, 9(8):e1001127, 2011.
- [2] Sustainable fisheries and aquaculture for food security and nutrition. <https://www.fao.org/3/i3844e/i3844e.pdf>.
- [3] ARPA-E. SEA-CO2: Sensing Exports of Anthropogenic Carbon through Ocean Observation. [https://arpa-e.energy.gov/sites/default/files/inlin e-files/ARPA-ESlide-SimonandDan\\_0.pdf](https://arpa-e.energy.gov/sites/default/files/inlin e-files/ARPA-ESlide-SimonandDan_0.pdf).
- [4] DARPA. Ocean of Things Aims to Expand Maritime Awareness across Open Seas. <https://www.darpa.mil/news-events/2017-12-06>, 2017.
- [5] Tidal X. Protecting the ocean with technology systems while feeding humanity sustainably. <https://x.company/projects/tidal/>.
- [6] Subsea pipeline monitoring – wireless intelligence made easy. <https://www.sonardyne.com/subsea-pipeline-monitoring-wireless-i ntelligence-made-easy/>, 2020. Sonardyne.
- [7] Jeff Tollefson. Sensor array provides new look at global ocean current. *Nature*, 2018.
- [8] Stephen C Riser, Howard J Freeland, Dean Roemmich, Susan Wijffels, Ariel Troisi, Mathieu Belbéoch, Denis Gilbert, Jianping Xu, Sylvie Pouliquen, Ann Thresher, et al. Fifteen years of ocean observations with the global argo array. *Nature Climate Change*, 6(2):145–153, 2016.
- [9] Michael Ho, Sami El-Borgi, Devendra Patil, and Gangbing Song. Inspection and monitoring systems subsea pipelines: A review paper. *Structural Health Monitoring*, 19(2):606–645, 2020.
- [10] Aquaculture Intelligence. <https://www.innovasea.com/aquaculture-i ntelligence/>, 2020. INNOVASEA.
- [11] Microsoft finds underwater datacenters are reliable, practical and use energy sustainably. <https://news.microsoft.com/source/features/susta inability/project-natick-underwater-datacenter/>, 2020. Sonardyne.
- [12] Junsu Jang and Fadel Adib. Underwater backscatter networking. In *Proceedings of the ACM Special Interest Group on Data Communication*, pages 187–199, 2019.
- [13] Reza Ghaffarivardavagh, Sayed Afzal, Osvaldo Rodriguez, and Fadel Adib. Ultra-wideband underwater backscatter via piezoelectric metamaterials. In *Proceedings of the ACM Special Interest Group on Data Communication*, 2020.
- [14] Sayed Saad Afzal, Waleed Akbar, Osvaldo Rodriguez, Mario Doumet, Unsoo Ha, Reza Ghaffarivardavagh, and Fadel Adib. Battery-free wireless imaging of underwater environments. *Nature Communications*, 13(1):5546, Sep 2022.
- [15] Sayed Saad Afzal, Reza Ghaffarivardavagh, Waleed Akbar, Osvaldo Rodriguez, and Fadel Adib. Enabling higher-order modulation for underwater backscatter communication. In *Global Oceans 2020: Singapore–US Gulf Coast*, pages 1–6. IEEE, 2020.
- [16] Joshua D Griffin and Gregory D Durgin. Complete link budgets for backscatter-radio and rfid systems. *IEEE Antennas and Propagation Magazine*, 51(2):11–25, 2009.
- [17] Udo Karthaus and Martin Fischer. Fully integrated passive uhf rfid transponder ic with 16.7- $\mu$ w minimum rf input power. *IEEE Journal of solid-state circuits*, 38(10):1602–1608, 2003.
- [18] Rodney FW Coates and RFW Coates. *Underwater acoustic systems*. Springer, 1990.
- [19] Milica Stojanovic. On the relationship between capacity and distance in an underwater acoustic communication channel. *ACM SIGMOBILE Mobile Computing and Communications Review*, 11(4):34–43, 2007.
- [20] Pavel V Nikitin, KVS Rao, and Roberto D Martinez. Differential rcs of rfid tag. *Electronics letters*, 43(8):1, 2007.
- [21] COMSOL, Inc. COMSOL Multiphysics Reference Manual, version 5.0, 2014.
- [22] Charles H Sherman and John L Butler. *Transducers and arrays for underwater sound*, volume 4. Springer, 2007.
- [23] W. James Trott. Sensitivity of piezoceramic tubes, with capped or shielded ends, above the omnidirectional frequency range. *The Journal of the Acoustical Society of America*, 62(3):565–570, September 1977.
- [24] S Orfanidis. Electromagnetic waves and antennas (sophocles j. orfanidis, 2016). URL <https://books.google.com.au/books>.
- [25] Ashley D Waite. *Sonar for practising engineers*. Wiley, 2002.
- [26] Milica Stojanovic, Josko Catipovic, and John G Proakis. Adaptive multichannel combining and equalization for underwater acoustic communications. *The Journal of the Acoustical Society of America*, 94(3):1621–1631, 1993.
- [27] Heui-Seol Roh, Alexander Sutin, and Barry Bunin. Determination of acoustic attenuation in the hudson river estuary by means of ship noise observations. *The Journal of the Acoustical Society of America*, 123(6):EL139–EL143, 2008.
- [28] Sonja Amoser, Lidia Eva Wysocki, and Friedrich Ladich. Noise emission during the first powerboat race in an alpine lake and potential impact on fish communities. *The Journal of the Acoustical Society of America*, 116(6):3789–3797, 2004.
- [29] Benthowave BII-7511 transducer. <https://www.benthowave.com/products/Specs/BII-7511Datasheet.pdf>.
- [30] BTech Acoustics BT-2RCL transducer. <http://www.btechacoustics.com/products/bt-2rcl>.
- [31] GeoSpectrum Technologies M27-931 transducer. <https://geospectrum.ca/wp-content/uploads/2021/05/M27-931-v2.pdf>.
- [32] RJ Bobber. Underwater electroacoustic measurements. Technical Report AD0717318, Naval Research Laboratory, 1971.
- [33] Steminc Piezo Ceramic Cylinder 54.1x47x40mm 17 KHz. <https://www.steminc.com/PZT/en/piezo-ceramic-cylinder-541x47x40mm-17-khz>.
- [34] Crown XLI 3500. <https://www.crownaudio.com/en/products/xli-3500>, 2018. XLI.
- [35] usrp n210. <http://www.ettus.com>, 2018. ettus inc.
- [36] Reson TC4014 Hydrophone. <http://www.teledynemarine.com/reson-t c-4014>.
- [37] Rigol Oscilloscope. <https://www.rigolna.com/products/digital-oscillo scopes/dho1000/>, 2023. Rigol.
- [38] Keysight N2791A probe. <https://www.keysight.com/us/en/product/N 2791A/high-voltage-differential-probe-25-mhz.html>, 2023. keysight.
- [39] ZXP Impedance Analyzer. <http://www.zxptest.com/eng/product/131>.
- [40] TDK RM6 ferrite core. [https://www.tdk-electronics.tdk.com/inf/80/db /fer/rm\\_6.pdf](https://www.tdk-electronics.tdk.com/inf/80/db /fer/rm_6.pdf).
- [41] Richard A Roberts and Clifford T Mullis. *Digital signal processing*. Addison-Wesley Longman Publishing Co., Inc., 1987.
- [42] Alan V Oppenheim. *Discrete-time signal processing*. Pearson Education India, 1999.
- [43] WHOI Micromodem 2. <https://acomms.whoi.edu/micro-modem/>, 2022. WHOI.
- [44] Angela D’amico and Richard Pittenger. A brief history of active sonar. Technical report, SPACE AND NAVAL WARFARE SYSTEMS CENTER SAN DIEGO CA, 2009.
- [45] BII-7550 Series Split Beam Transducer. <https://www.benthowave.com /products/Specs/BII-7550Datasheet.pdf>, 2022. Benthowave.
- [46] James Preisig. Acoustic propagation considerations for underwater acoustic communications network development. *ACM SIGMOBILE Mobile Computing and Communications Review*, 11(4):2–10, 2007.
- [47] Pavel V Nikitin and KV Seshagiri Rao. Theory and measurement of backscattering from rfid tags. *IEEE Antennas and Propagation Magazine*, 48(6):212–218, 2006.
- [48] Peter Oppermann and Christian Renner. Higher-order modulation for acoustic backscatter communication in metals. In *Proceedings of the ACM SIGCOMM 2022 Conference*, pages 576–587, 2022.
- [49] Zheng Gong, Lubing Han, Zhenlin An, Lei Yang, Siqi Ding, and Yu Xi- ang. Empowering smart buildings with self-sensing concrete for structural health monitoring. In *Proceedings of the ACM SIGCOMM 2022 Conference*, pages 560–575, 2022.

- [50] Ahmed Allam. *Acoustic Power Transfer Leveraging Piezoelectricity and Metamaterials*. PhD thesis, Georgia Institute of Technology, Atlanta, GA, July 2021.
- [51] Ting Chia Chang, Marcus J. Weber, Jayant Charhad, Spyridon Baltasavias, and Amin Arbabian. End-to-End Design of Efficient Ultrasonic Power Links for Scaling Towards Submillimeter Implantable Receivers. *IEEE Transactions on Biomedical Circuits and Systems*, 12(5):1100–1111, October 2018.
- [52] Mohammad Meraj Ghanbari, David K. Piech, Konlin Shen, Sina Faraji Alamouti, Cem Yalcin, Benjamin C. Johnson, Jose M. Carmena, Michel M. Mahabiz, and Rikky Muller. A Sub-mm3 Ultrasonic Free-Floating Implant for Multi-Mote Neural Recording. *IEEE Journal of Solid-State Circuits*, 54(11):3017–3030, November 2019.
- [53] Mohammad Meraj Ghanbari and Rikky Muller. Optimizing Volumetric Efficiency and Backscatter Communication in Biosensing Ultrasonic Implants. *IEEE Transactions on Biomedical Circuits and Systems*, 14(6):1381–1392, December 2020.
- [54] Milica Stojanovic and James Preisig. Underwater acoustic communication channels: Propagation models and statistical characterization. *IEEE communications magazine*, 47(1):84–89, 2009.
- [55] Raffaele Guida, Emrecan Demirors, Neil Dave, Jennie Rodowicz, and Tommaso Melodia. An acoustically powered battery-less internet of underwater things platform. In *2018 Fourth Underwater Communications and Networking Conference (UComms)*, pages 1–5. IEEE, 2018.
- [56] Alper Bereketli and Semih Bilgen. Remotely powered underwater acoustic sensor networks. *IEEE Sensors Journal*, 12(12):3467–3472, 2012.
- [57] Alper Bereketli. Interference-free source deployment for coverage in underwater acoustic backscatter networks. *Peer-to-Peer Networking and Applications*, 15(3):1577–1594, 2022.
- [58] Boris Aronov. The energy method for analyzing the piezoelectric electroacoustic transducers. *The Journal of the Acoustical Society of America*, 117(1):210–220, January 2005.
- [59] Thomas L. Szabo. *Diagnostic Ultrasound Imaging: Inside Out*. Academic Press, 2nd edition edition, December 2013.
- [60] Ahmed Allam, Karim Sabra, and Alper Erturk. Piezoelectric transducer design for simultaneous ultrasonic power transfer and backscatter communication. *Smart Materials and Structures*, 31(9):095003, July 2022.
- [61] Prakhar Srivastava, Brendan Nichols, and Karim G Sabra. Passive underwater acoustic markers using bragg backscattering. *The Journal of the Acoustical Society of America*, 142(6):EL573–EL578, 2017.
- [62] Joe Roman, Irit Altman, Meagan M Dumphry-Daly, Caitlin Campbell, Michael Jasny, and Andrew J Read. The marine mammal protection act at 40: status, recovery, and future of us marine mammals. *Annals of the New York Academy of Sciences*, 1286(1):29–49, 2013.